

11,01

Formation of a dendrite structure in crystals NiFeGaCo alloy in the process of growing by the Stepanov method

© Yu.G. Nosov, V.M. Krymov, M.G. Vasiliev, A.V. Chikiryaka, V.I. Nikolaev

Ioffe Institute,
St. Petersburg, Russia
E-mail: v.krymov@mail.ioffe.ru

Received July 13, 2021

Revised July 13, 2021

Accepted July 15, 2021

The process of growing crystals of the NiFeGaCo alloy by the Stepanov method has been developed. It was found that the structural perfection is disturbed by the formation of dendrites, which are distributed inhomogeneously both along the length and in the cross sections of the crystals. The blocking effect of the dendrites on growth crystals of the martensite phase, which appears when the samples are cooled to the temperature of the transition of the crystal to the martensite state, is found. The elemental composition of dendritic formations was studied and it was shown that the iron content in the dendrite is approximately 30% higher, and the gallium content is 40% lower than in the matrix. Based on the modeling of heat transfer processes in the real growth zone, taking into account the experiments performed, recommendations were obtained for suppressing the formation of dendrites

Keywords: Dendritic structure, shape memory alloys, Stepanov's method.

DOI: 10.21883/PSS.2022.14.54345.167

1. Introduction

In recent decades the ferromagnetic nickel Heusler alloys with shape memory effect (SME) and, particularly, NiFeGaCo are studied intensively by many researchers [1–5]. These crystals are interesting due to possibility of obtaining the large reversible magnetically-induced deformations, superelasticity (SE), and effect of high-speed recovery of shape memory deformation (HSROSMD).

Most of NiFeGaCo crystals are grown for research purposes using Bridgman method [6]. When examining this technology in terms of further practical application, it is obvious, that small sizes of obtained samples will be insufficient for most drive designs [7]. The next logical step of studies, in our opinion, should be the development of technology for obtaining such crystals with larger length and various specified cross section, that will broaden the design capabilities to create devices based on effects of shape memory, SE and HSROSMD. Examples of creation of devices based on profiled crystals of CuAlNi with SME, obtained using Stepanov method, are demonstrated in [8,9]. Earlier we demonstrated, that NiFeGaCo monocrystals can be grown from melt using industrial methods, e.g., Czochralski and Stepanov methods, that allow to obtain the high-quality crystals of silicon [10] and sapphire [11]. By now, using Stepanov method we obtained crystals, from which it is possible to create samples, comparable with those, that are cut from ingots, grown using Bridgman method [12–15].

However, the problem of heterogeneity of composition and structure of grown crystals prevents from fully-featured implementation of functional capabilities of NiFeGaCo

crystals. Particularly, we faced with formation of dendrites in monocrystal matrix during crystals growing.

It should be noted, that dendritic structure formation is rather common phenomenon during crystallization of metal alloys based on iron and nickel [16–21]. Dendrites — a structural defect of characteristic skeletal shape, consisting of a central branch (main axis) and side branches, perpendicular to it. Dendritic structure is formed directly at crystallization front and then remains regardless of further heat treatments, such as high-temperature annealing and quenching [22].

The purpose of this work is to study the reasons of dendritic structure formation in crystals of Ni₄₉Fe₁₈Ga₂₇Co₆ alloy at their growing and its influence on functional properties of crystals, optimization of crystallization modes for dendrites formation suppression.

2. Experiment

2.1. Crystals growing using Stepanov method

Using Stepanov method, the crystals of Ni₄₉Fe₁₈Ga₂₇Co₆ composition were grown as cylindrical rods, diameter of which was set by a die, from the melt per seed, crystallographically oriented towards [100]. Growing was performed from alundum melting crucible at setup with induction heating with pulling rate of 1 mm/min under argon atmosphere. Crystals with a length of up to 250 mm and diameter of 6 mm were grown. Scheme of thermal zone and photo of a crystal during growing are presented in Fig. 1.

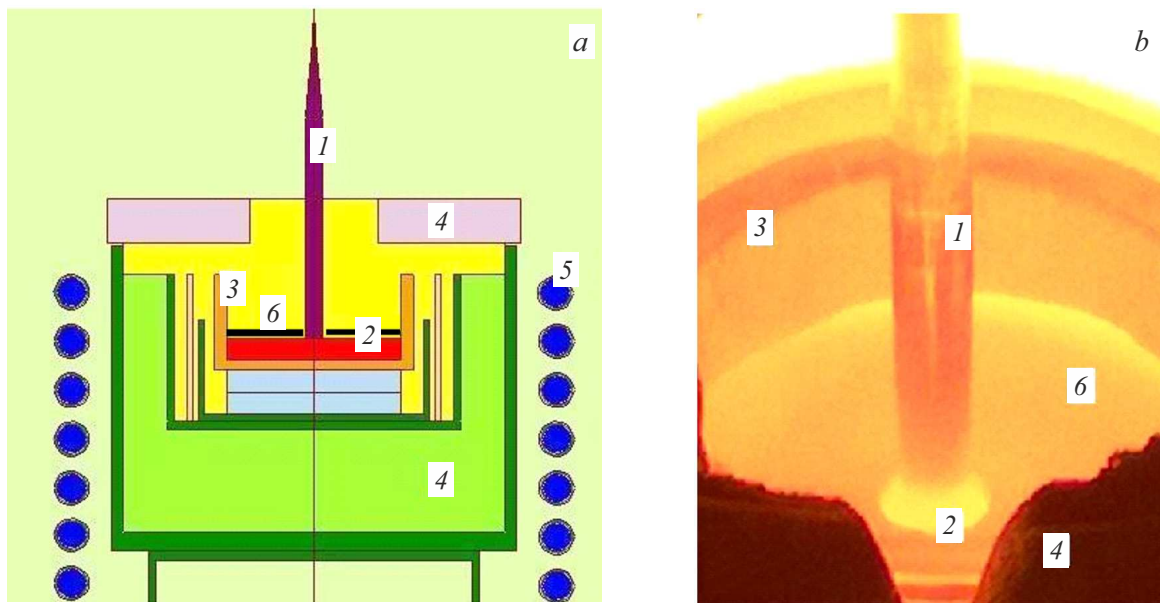


Figure 1. Scheme of thermal zone (a) and photo of a crystal during growing (b): 1 — crystal, 2 — melt, 3 — melting crucible, 4 — thermal insulation, 5 — inducer, 6 — die.

2.2. Determination of martensitic transformation temperature

For accurate determination of temperature of austenite transition into martensite M_S the washer-shaped sample with polished surface was put into a thermostat. Cooling was performed with very low rate: ~ 0.04 K/min. The polished end surface of the sample was monitored and photographed. Temperature of martensitic transformation start was defined by the first martensite crystals appearing on the end surface. Under these conditions the martensite structure is formed and developed in crystal within temperature range of 9.5 – 9.0°C . Time from the first martensite needles appearing to their propagation over the whole cross section was about 18 min. The reverse transition of martensite — austenite was performed at heating to $A_s \approx 15$ – 16°C . Phase transition temperatures were defined on crystals of $\text{Ni}_{49}\text{Fe}_{18}\text{Ga}_{27}\text{Co}_6$, cut from dendrite-free regions. The further study was performed on as grown crystals without any additional heat treatment.

2.3. Crystal defect structure study

Crystal structure was studied on three washers, cut from the grown crystal at distances of 15, 100 and 160 mm from the seed. For dendritic structure observing these samples were polished and chemically etched in solution, consisting of three quarters of nitric acid and one quarter of hydrochloric acid. Structure details were studied using optical microscope Carl Zeiss Jena Amplitval and scanning electron microscope Phenom PROX.

Figure 2, a shows the photo of a cross section in 15 mm from the seed. It is seen, that dendrites are distributed

along cross section non-uniformly: in the central part the density of dendrites N is low, on the edges — significantly higher. In the central region of the crystal, inside a square 2×2 mm, the value N is 10–15 dendrites per mm^2 . For a region near the crystal edge the value can be evaluated as $N \approx 50$ dendrites per mm^2 . Dendrites sizes are changing over wide range: from hundredths of mm to 0.5–1 mm. It should be noted, that all photos in Fig. 2 (upper row) are made at room temperature, when the crystal is in austenitic state.

Figure 2, b shows the crystal surface at a distance of 100 mm from the seed. The total number of dendrites in this cross section is almost half as much, as in the cross section in Fig. 1, a. Dendrites distribution is significantly non-uniform: the upper part of cross section contains the biggest number of dendrites. Figure 2, c shows the cross section picture at a distance of 160 mm from the seed. In this cross section the selective etching demonstrated a total lack of dendrites.

These data show, that defect structure of the crystal is heterogeneous in terms of cross section and length of the ingot. Maximum concentration of dendrites was observed in the initial crystal part, closer to the seed, and from there it gradually reduced and at a distance of about 160 mm from the seed there were no dendrites at all.

For studying the structure of samples at martensitic transformation all three samples were cooled below temperature of M_S . On the first sample (Fig. 2, d), only original dendrite picture was observed on the first sample and there were no characteristic needles of martensite crystals. On the second sample (100 mm from the seed) the dendrites and martensite needles are simultaneously observed, while the

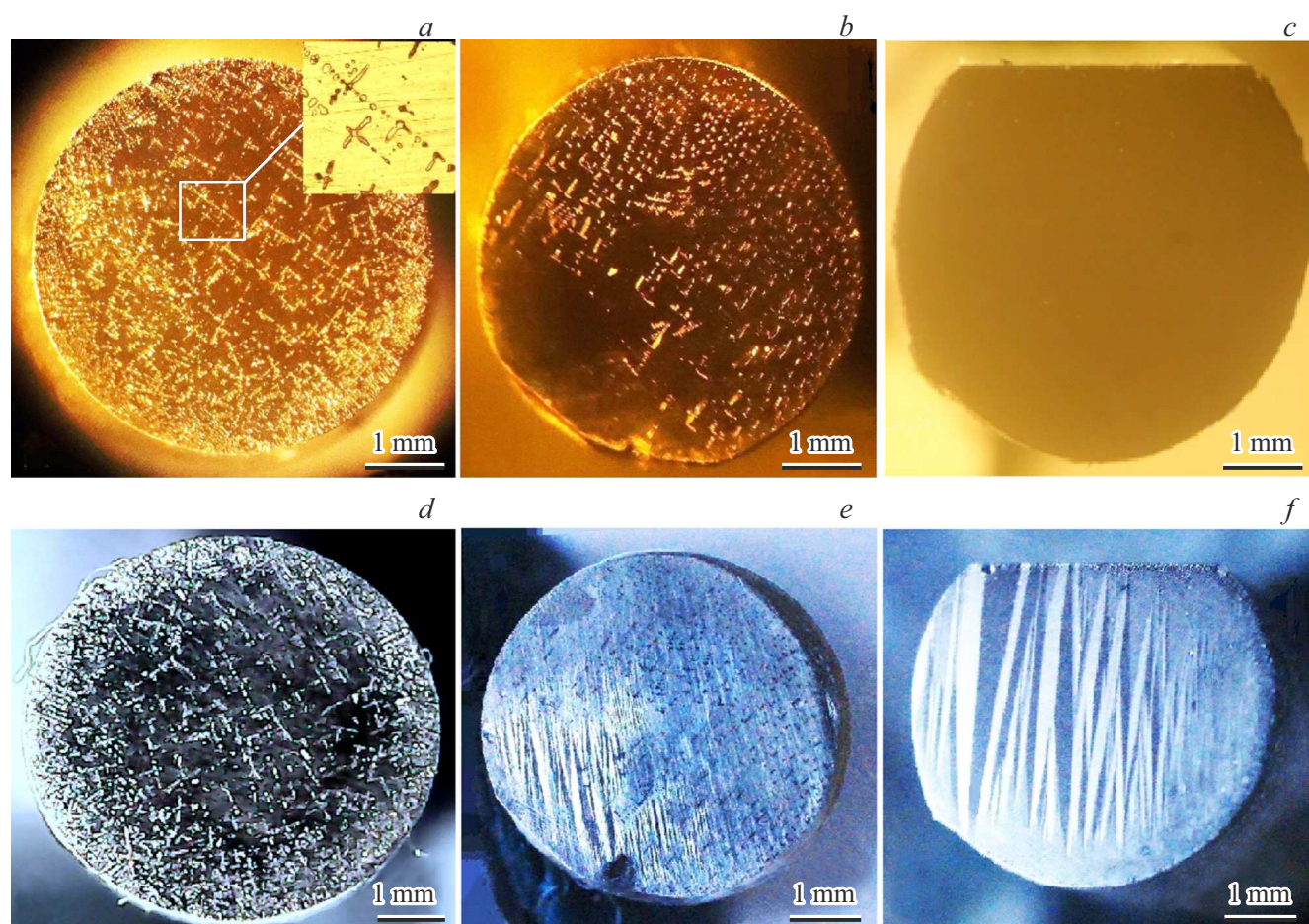


Figure 2. Photos of thin cross sections of $\text{Ni}_{49}\text{Fe}_{18}\text{Ga}_{27}\text{Co}_6$ crystal at a distance of 15 mm (*a* and *d*), 100 mm (*b* and *e*) and 160 mm (*c* and *f*) from the seed. The upper row of photos — at room temperature (austenite phase), lower — at cooling below point of transition into martensitic state.

biggest number of martensite needles is in lower, dendrite-free part of the cross section (Fig. 2, *e*). And finally, on the third sample, where were no dendrites at all, we observe the large martensite crystals over the whole cross section (Fig. 2, *f*).

Thus, at crystal cooling below temperature of M_S the martensite crystals appeared only in those surface sections, where were no dendrites.

2.4. Martensitic transformation in crystal with dendrites

By cooling a crystal, not containing dendrites, you can usually observe the following pattern of martensite development. Upon reaching temperature of M_S the martensite needles appeared on the crystal edge and quickly filled the whole crystal cross section. Another pattern is observed, if crystal contains dendrites. In this case the formation of martensite crystals, reaching the group of dendrites or a single big dendrite, stops and does not move through

dendrites. Example of martensite needles stop in front of single dendrites is presented in Fig. 3.

These photos show two big dendrites in cross section of $\text{Ni}_{49}\text{Fe}_{18}\text{Ga}_{27}\text{Co}_6$ crystal at room temperature (Fig. 3, *a*) and the same two dendrites surrounded by martensite needles at crystal cooling to temperature of M_S (Fig. 3, *b*). It is seen, that martensite needles, coming to dendrites from different directions, can not pass through them. I.e. dendrites act as stoppers at martensite phase propagation in crystals.

2.5. Elemental composition of dendrites

Elemental composition of dendrites and regions between them was defined at scanning electron microscope Phenom PROX with integrated energy dispersive spectroscopy (EDS) system. The electron irradiation beam diameter was $\sim 3\ \mu\text{m}$. Measurement results, presented in Table 1, showed, that along crystal length, not considering dendrites, the composition changed insignificantly and corresponds to initial composition of $\text{Ni}_{49}\text{Fe}_{18}\text{Ga}_{27}\text{Co}_6$.

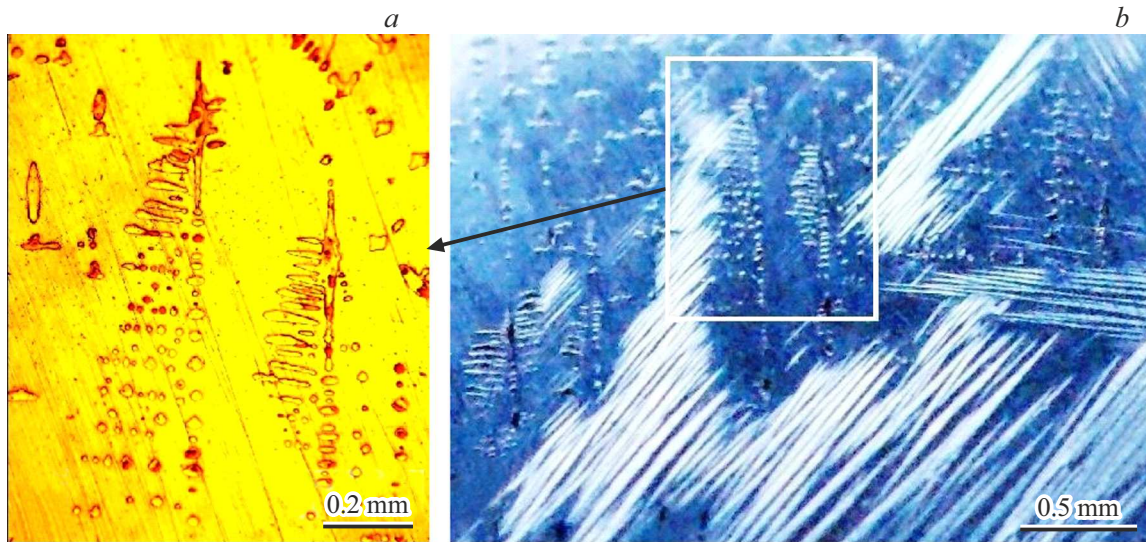


Figure 3. Photos of a cross section of Ni₄₉Fe₁₈Ga₂₇Co₆ crystal with characteristic dendrites: (a) at room temperature in austenitic state, (b) the same sample is cooled to a point of a start of transition from austenite to martensite M_s . Box in Fig. 3, b shows the same section of the crystal surface as in Fig. 3, a.

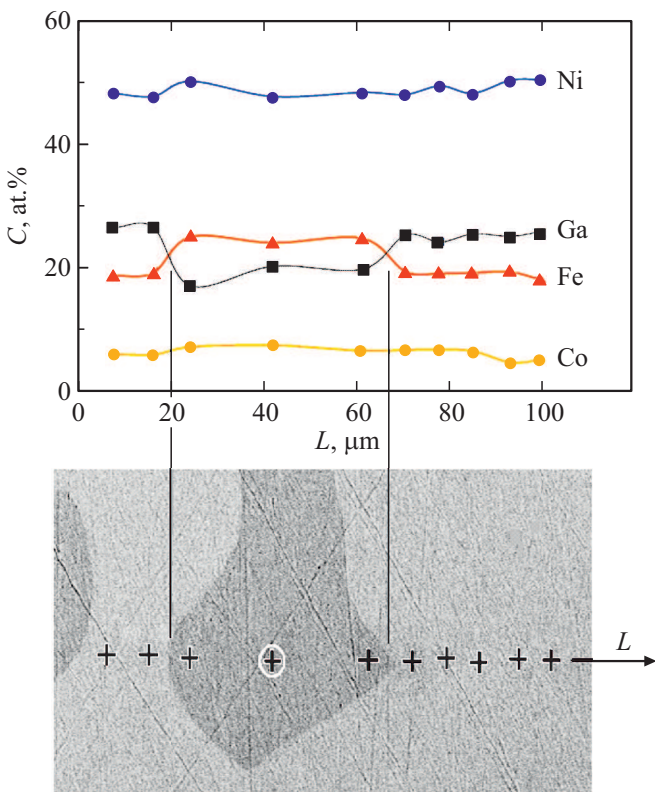


Figure 4. Distribution of elemental composition in dendrite region.

More precise measurements in dendrites region showed, that elemental composition of dendrite body differs from composition of surrounding matrix and iron content in dendrite is always higher, while gallium is less, than outside

of it. Figure 4 shows the example of measurement of elemental composition in dendrite and near it. It is seen, that iron content in dendrite is almost by 30% higher, while gallium content is almost by 40% less, than in regions, adjacent to dendrite. Nickel and cobalt content does not show any significant jump at dendrites boundary.

3. Modeling of growing process

What is the reason of the observed structure heterogeneity of dendrites density distribution along crystal length? Since it is known, that dendrites are formed directly at crystallization front, this heterogeneity can be caused either by change of the melt chemical composition, or by change of thermal conditions during growing. The first reason is unlikely, since direct measurements (Table 1) showed, that composition changes insignificantly. The most probable is the second reason. Since experimental measurements of temperature distributions in growing zone are complicated and labor intensive, the mathematical modeling of heat and mass transfer processes in real thermal zone was used. It allowed to study the influence of parameters of growth and thermal zone configuration on the melt hydrodynamics and temperature distribution in the growing crystal. This method can also optimize thermal zone for dendrite growth suppression, growing of crystals with various cross section and achieving the maximum process performance.

Modeling was performed using BasicCGSim software package for the real thermal zone with induction heating. Calculations were made for the case of growing a crystal with diameter of 6 mm by Stepanov method using die with cylindrical hole. Growth rate was 60 mm/h for the basic design case. Crystallization temperature was taken

Table 1. Elemental composition of crystals at various distances from the seed

| Element | Content, at.% | | |
|---------|---------------------|----------------------|----------------------|
| | 15 mm from the seed | 100 mm from the seed | 160 mm from the seed |
| Ni | 47.4 | 49.0 | 49.1 |
| Fe | 18.8 | 19.1 | 19.6 |
| Ga | 27.4 | 25.5 | 24.8 |
| Co | 6.4 | 6.4 | 6.5 |

as 1600 K. Temperature distributions in the melt, crystal, as well as hydrodynamics of the melt flow in crucible were calculated for the succeeding growth stages along the crystal length of 50, 100 and 160 mm. Figure 5 shows the patterns of isotherms and melt flow lines at crystal length of 160 mm. It is seen, that the melt in the crucible is actively mixed, moving through spiral from hot walls of the crucible upwards and going downwards in the center of the

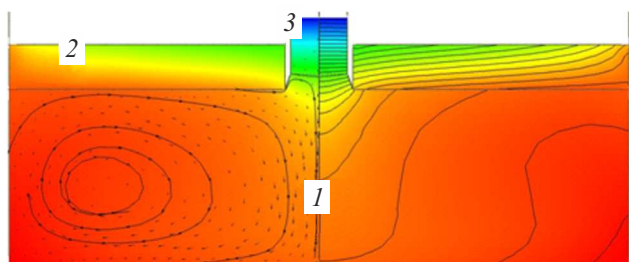


Figure 5. Pattern of isothermal lines with interval of 1 K (on the right) and melt flow lines (on the left) at crystal growing using Stepanov method. 1 — melt, 2 — die, 3 — crystal.

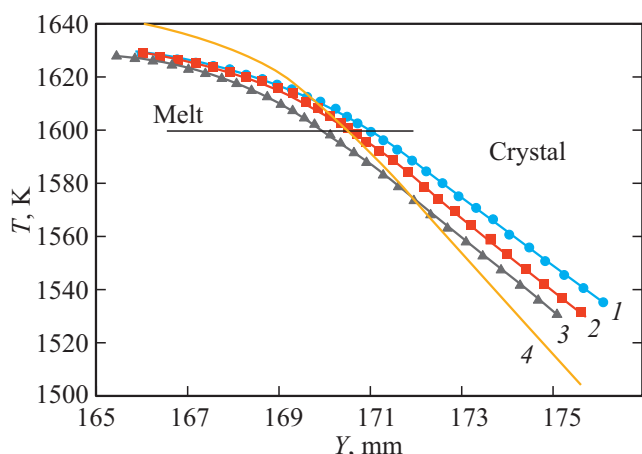


Figure 6. Temperature distribution near crystallization front in the melt and along crystal axis at growing using Stepanov method at various growth stages: 1, 2 and 3 — crystals, reached a length of 50, 100 and 160 mm, 4 — calculation for crystal length of 100 mm in thermal zone without top cover. Crystallization temperature of 1600 K is designated with horizontal line.

crucible. Figure 6 shows the temperature distribution along growing axis at crystal length of 50, 100 and 160 mm. The performed modeling calculations showed small influence of pulling rate change in a range from 10 to 240 mm/h on temperature distribution. It should be noted, that modeling allowed to define such an important parameters of crystallization process as temperature gradients at the crystallization front. It is very hard to do it experimentally. Calculations show, that with crystal length increase the temperature gradient in the melt at crystallization front increases from 6.9 K/mm to 9.7 K/mm.

4. Discussion

4.1. Analysis of dendrite structure formation

Thus, the correlation between temperature gradient increase in the melt at the front and dendrites formation disappearing is observed. This corresponds to classical concepts of dendrite structure formation at concentration undercooling of the melt. As per [23], the criterion of transition from cellular and dendritic growth to normal (planar) is increase of parameter G_L/V , where G_L — temperature gradient in the melt at crystallization front, and V — growing rate. Increase of temperature gradient results in decrease of liquid-solid zone height at crystallization front, where dendritic structure is actually formed. On the other side, increase of growing rate results in increase of undercooling under crystallization front, thus increasing the probability of dendritic structure forming. Connection of parameter G_L/V and dendritic structure formation was observed in many crystallization processes. For instance, in the work [18] for obtaining the crystals of ferromagnetic alloy of $\text{Co}_{37}\text{Ni}_{34}\text{Al}_{29}$ the method of direct crystallization with high temperature gradient was used. Presence or absence of dendrites in the grown crystals was connected with value of parameter G_L/V . Developers of heat-resistant nickel alloys faced the similar problems of dendrites formation in castings structure. In this case the method of direct crystallization [24,25] was used for obtaining the turbine blades blanks. These works results and our data are presented in Table 2.

From the presented data it is seen, that dendrites formation at crystallization correlates with parameter G_L/V .

Table 2. Correlation of crystallization parameter G_L/V (G_L — temperature gradient, V — growth rate) and dendritic structure in alloys

| G_L , K/mm | V , mm/s | G_L/V , Ks/mm ² | Dendrites | Reference |
|--------------|------------|------------------------------|-----------|-----------|
| 80 | 0.015 | 5333 | No | [18] |
| 80 | 0.15 | 533 | Yes | [18] |
| 10–12 | 0.0017 | 100–120 | No | [24] |
| 10–12 | 0.005 | 30–40 | Yes | [24] |
| 10.3 | 0.017 | 606 | No | Our data |
| 9 | 0.017 | 529 | Yes | Our data |

To prevent from dendrites formation it is necessary to increase temperature gradient at crystallization front and decrease growth rate.

4.2. Changes of dendrites elemental composition

The observed results on chemical analysis of dendrites are in good agreement with the already known data on dendrites in steels [22]. For multi-component steels it was shown, that dendrites are enriched with the highest melting component. In our case for composition of Ni₄₉Fe₁₈Ga₂₇Co₆ this component is iron (melting temperature is 1539°C).

Change of elemental composition of dendrites was also observed at crystallization of other alloys with SME. For instance, in [21] the elemental mapping using electron scanning microscope in Ni₅₂Fe₂₀Ga₂₆Co₂ alloy revealed increase of iron and cobalt content in dendrite and decrease of gallium content compared to surrounding matrix. Similar result in terms of these elements change was also observed in [16].

4.3. Dendritic structure influence on martensitic transformation

Effect of martensite needles stop at dendrites, observed during our studies, is of decisive interest. In compounds like NiFeGaCo in austenitic state the basic phase has BCC lattice of $L2_1$ and disordered γ -phase (or dendrites) with FCC lattice, described in many works [17]. At phase transformation of austenite \rightarrow martensite the basic phase transitions into face-centered tetragonal lattice of martensite $L1_0$, while in γ -phase the FCC lattice remains [26]. Besides, according to our measurements, dendrite has elemental composition, different from matrix, where martensitic transformation temperature is strongly displaced or there is no transformation at all. Actually, it is a foreign inclusion in NiFeGaCo crystal matrix, completely blocking or complicating the martensite crystals movement. If there are dendrites, not the whole crystal volume participates in martensitic transformation. At very high dendrite density, like, for instance, in the

sample near the seed (Fig. 2, *a, d*) the regions between separate dendrites can be less than critical, required for lattice reconfiguration into martensite phase [27].

5. Conclusions

1. The long profiled crystals of Ni₄₉Fe₁₈Ga₂₇Co₆ with diameter of 6 and length of up to 250 mm with shape memory effect are grown from the melt using Stepanov method.

2. It is shown, that structure heterogeneity along the length and cross sections of these crystals is mainly related to dendritic structure, formed at crystallization front.

3. Chemical composition of dendrites differs from the crystal matrix composition, iron content in dendrite is almost by 30% higher, while gallium content — almost by 40% less and is within region of compositions without SME.

4. It is shown, that dendrites also prevent from martensite crystals growing in matrix of Ni₄₉Fe₁₈Ga₂₇Co₆ at martensite transformations in thermal cycles.

5. Modeling of crystallization process of these crystals using Stepanov method indicates, that for dendrites formation suppression and obtaining the dendrite-free crystals it is necessary to change the growth zone design to increase temperature gradient at crystallization front and at the same time to decrease the crystals pulling rate.

Acknowledgments

The authors would like to thank S.A. Pul'nev for help with the work with setup and useful discussions.

Conflict of interest

The authors declare that they have no conflict of interest.

References

- [1] Heusler Alloys, Properties, Growth, Applications / Ed. C. Felser, A. Hirohata, Springer International Publishing, Switzerland (2016). 486 p.
- [2] V.D. Buchel'nikov, A.N. Vasil'ev, V.V. Koledov, S.V. Taskaev, V.V. Hovajlo, V.G. Shavrov. UFN **176**, 8, 900 (2006) (in Russian).
- [3] V.I. Nikolaev, S.I. Stepanov, P.N. Yakushev, V.M. Krymov, S.B. Kustov. Intermetallics **119**, 1 (2020).
- [4] E.Yu. Panchenko, E.E. Timofeeva, N.G. Larchenkova, Yu.I. Chumlyakov, A.I. Tagiltsev, H.J. Maier, G. Gerstein. Mater. Sci. Eng. A **706**, 95 (2017).
- [5] V.I. Nikolaev, P.N. Yakushev, G.A. Malygin, S.A. Pul'nev. PZhTF **36**, 19, 83 (2010) (in Russian).
- [6] R.F. Hamilton, H. Schitogly, C. Efstathiou, H.J. Maier. Acta Mater. **55**, 4867 (2007).
- [7] J. Jani, M. Leary, A. Subic. J. Intell. Mater. Syst. Struct. **28**, 13, 1699 (2017).
- [8] S.A. Pul'nev, A.I. Pryadko, S.G. Yastrebov, V.I. Nikolaev. ZhTF **88**, 6, 843 (2018) (in Russian).

- [9] A.I. Pryadko, A.V. Chikiryaka, S.A. Pul'nev. ZhTF **89**, 12, 1880 (2019) (in Russian).
- [10] J.K. Kearns. Silicon single crystals. In: Single Crystals of Electronic Materials Growth and Properties / Ed. R. Fornari. Elsevier Ltd (2019). P. 5.
- [11] P.I. Antonov, V.N. Kurlov. Prog. Cryst. Growth Charact. Mater. **44**, 63 (2002).
- [12] A.I. Averkin, V.M. Krymov, L.I. Guzilova, R.B. Timashov, A.V. Soldatov, V.I. Nikolaev. PZhTF **44**, 3 (2018) (in Russian).
- [13] Yu.G. Nosov, A.V. Soldatov, V.M. Krymov, S.A. Pul'nev, V.I. Nikolaev. PZhTF **45**, 2729 (2019) (in Russian).
- [14] G.A. Malygin, V.I. Nikolaev, V.M. Krymov, S.A. Pul'nev, S.I. Stepanov. ZhTF **89**, 873 (2019) (in Russian).
- [15] S. Belyaev, N. Resnina, V.I. Nikolaev, R.B. Timashov, A. Savelieva, A. Gazizullina, V.M. Krymov, A. Sibirev. J. Mater. Eng. Perform. **28**, 7, 4234 (1918).
- [16] K. Oikawa, T. Omori, Y. Sutou, H. Morito, R. Kainuma, K. Ishida. Met. Mater. Trans. A **38**, 767 (2007).
- [17] J. Liu, N. Scheerbaum, D. Hinz, O. Gutfleisch. Acta Mater. **56**, 3177 (2008).
- [18] J.Z. Li, B. Huang, J.G. Li. J. Cryst. Growth **317**, 110 (2011).
- [19] Q. Liu, J. Liu, Y. Huang, Q. Hua, J. Li. J. Alloys Compd. **572**, 186 (2013).
- [20] P. Jiang, J. Bai, P. Wei, S. Han, M. Yang, F. Teng, X. Wang, X. Zhao. Mater. Sci. Forum **879**, 2061 (2017).
- [21] G. Gurau, C. Gurau, F. Tolea, V. Sampath. Materials **12**, 1939, 1 (2019).
- [22] I.N. Golikov, S.B. Maslenkov. Dendritnaya likvatsiya v stalyakh i splavakh. Metallurgiya, M. (1977) (in Russian).
- [23] B. Chalmers. Principles of Solidification. John Wiley, N.Y. (1964). 319 p.
- [24] E.N. Kablov, V.N. Tolorajya, I.M. Demonis, N.G. Orekhov. Tekhnologiya legkikh splavov **2**, 60 (2007) (in Russian).
- [25] E.M. Visik, V.V. Gerasimov, E.V. Kolyadov, E.V. Filonova. Zavod. laboratoriya. Diagnostika materialov. **84**, 6, 38 (2018) (in Russian).
- [26] K. Oikawa, T. Ota, Y. Sutou, T. Ohmori, R. Kainuma, K. Ishida. Mater. Transact. **43**, 9, 2360 (2002).
- [27] G.A. Malygin. FTT **61**, 7, 1310 (2019) (in Russian).